Initial Results of a Positron Tomograph for Prostate Imaging

J. S. Huber, *Member, IEEE,* W.S. Choong, *Member, IEEE,* W. W. Moses, *Senior Member, IEEE,* J. Qi, *Member, IEEE,* J. Hu, *Member, IEEE,* G.C. Wang, *Member, IEEE,* D. Wilson, S. Oh, R. H. Huesman, *Fellow, IEEE,* S. E. Derenzo, *Fellow, IEEE,* and T. F. Budinger, *Member, IEEE*

Abstract—We present the status and initial images of a positron tomograph for prostate imaging that centers a patient between a pair of external curved detector banks (ellipse: 45 cm minor, 70 cm major axis). The distance between detector banks adjusts to allow patient access and to position the detectors as closely as possible for maximum sensitivity with patients of various sizes. Each bank is composed of two axial rows of 20 CTI PET Systems HR+ block detectors for a total of 80 modules in the camera. Compared to an ECAT HR PET system operating in 3D mode, our camera uses about one-quarter the number of detectors and has approximately the same sensitivity for a central point source, because our detectors are close to the patient. The individual detectors are angled in the plane to point towards the prostate to minimize resolution degradation in that region. The detectors are read out by modified CTI data acquisition electronics. We have completed construction of the gantry and electronics, have developed detector calibration and data acquisition software, and are taking coincidence data. We demonstrate that we can clearly visualize a "prostate" in a simple phantom. Reconstructed images of two phantoms are shown.

I. Introduction

We present the development of a positron tomograph optimized to image the prostate. This instrument images radiopharmaceuticals that specifically localize in the prostate to confirm the presence, absence or progression of disease. It has approximately four times fewer detectors than an ECAT HR or HR+ PET scanner, which will reduce the cost and potentially increase clinical availability.

Prostate cancer has a prevalence and diagnostic rate similar to breast cancer, with 230,000 new cases diagnosed in the United States each year and one man in 6 diagnosed during his lifetime. Prostate cancer suspicion is typically based on an elevated prostate-specific antigen (PSA) level or a suspicious mass found during a digital rectal exam. Treatment decision is based mainly on biopsy confirmation of prostate cancer. Typical treatment options include prostatectomy, external beam irradiation, brachytherapy (interstitial implantation of radioactive seeds), androgen ablation (hormone) therapy, or "watchful waiting." A major problem with prostatic cancer therapy is the question of where to biopsy, when to treat, or whether to treat at all. This is particularly problematic in the case of an increased PSA level with non-diagnostic repeated biopsies or after a prostatectomy. A new imaging technology for sensitive detection of prostate cancer is needed to confirm initial diagnosis, guide biopsy and help guide treatment decisions. In addition, a new method is needed to assess response shortly after a treatment intervention.

In order to help meet these needs, we have built a PET camera optimized to image the prostate. Functional PET imaging will help detect malignant tumors in the prostate and/or prostate bed as a follow-up for an elevated PSA level, as well as possibly help determine tumor "aggressiveness" based on metabolic uptake levels. Although not optimized to detect distant metastatic disease, this PET camera should also image local spread beyond the prostate bed to help guide treatment decisions such as whether a narrow or wide irradiation treatment field is needed.

Promising PET radiopharmaceuticals have recently demonstrated outstanding results in the sensitive detection of prostate cancer, inspiring a new interest in using PET for prostate cancer imaging. Consistent with the evidence of increased pool size of choline in prostate cancer [1, 2], Hara and co-workers find that: [^{11}C]choline clears the blood faster than FDG; its uptake in prostate tumors is significantly higher than in normal and surrounding tissues [3, 4], providing excellent tumor/normal contrast; and bladder accumulation is minimal if the correct time course is chosen [5] which is a major advantage over FDG. Therefore, [^{11}C]choline is an attractive PET tracer for imaging primary and metastatic tumors of the prostate and potentially for other regions of the body [6-10]. Other ^{11}C radiopharmaceuticals are also under investigation for prostate cancer PET imaging, including [^{11}C]acetate and [^{11}C]methionine.

^{18}F imaging has the advantage of a longer half-life, which increases clinical utility because an on-site cyclotron facility would not be necessary (as it would for ^{11}C imaging). Although many groups have shown that PET imaging with [^{18}F]fluorodeoxyglucose (FDG) is not a good technique for prostate cancer diagnosis, there are several other ^{18}F

Manuscript received December 1, 2004. This work was supported in part by the Director, Office of Science, Office of Biological and Environmental Research, Medical Science Division of the U.S. Department of Energy under Contract No. DE-AC03-76SF00098, in part by Department of Defense grant number DAMD17-02-1-0081, and in part by National Institute for Biomedical Imaging and Bioengineering grant number R01 EB 00194.

J. S. Huber, W.S. Choong, W. W. Moses, J. Hu, D. Wilson, S. Oh, R. H. Huesman and S.E. Derenzo are with the Lawrence Berkeley National Laboratory, Mailstop 55-121, 1 Cyclotron Road, Berkeley, CA 94720 USA (telephone: 510-486-6445, e-mail: jshuber@lbl.gov). J. Qi is with the Department of Biomedical Engineering, University of California, Davis, CA 95616 USA (telephone: 530-754-6142, email: qi@ucdavis.edu).

radiopharmaceuticals currently under investigation including [^{18}F]fluorocholine (FCH) [11, 12]. PET images using [^{18}F]fluorocholine demonstrate high standardized uptake values (*e.g.*, SUV of 8), indicating that FCH is well localized in the prostate cancer and can be imaged with good resolution if short scan times (~five minutes) are used to avoid bladder background.

II. Camera Design

A. Overview

These new prostate tracers motivated us to build a low cost PET camera optimized to image the prostate. Coincidence imaging of positron emitters is achieved using a pair of external curved detector banks, one placed above and one below the patient. Fig. 1 shows the transaxial and sagittal views of the camera. The bottom bank is fixed below the patient bed, and the top bank moves upward for patient access and downward for maximum sensitivity. Each bank consists of two axial rows of 20 CTI ECAT HR+ block detectors (80 detectors total in the camera), forming two arcs with a minor axis of 45 cm and major axis of 70 cm. Our prostate camera has about one-fourth the number of detectors as an EXACT HR or HR+ because: (a) the patient is not fully encircled in 2D, (b) an elliptical shape is used instead of a circular one, and (c) the axial coverage is only 8 cm. However, since the average distance to the detectors is approximately one-half that of a conventional PET system, we expect to achieve improved detection efficiency at a lower cost.

Individual detector modules are angled to point towards the camera center near the prostate location in order to reduce penetration effects (in the detector) for annihilation photons originating in the prostate. This geometry increases resolution selectively in the region of the prostate and is an unique feature for a non-circular camera geometry. Annihilation photons from other parts of the field of view (FOV) will suffer increased penetration effects, but these regions are less important. Both detector banks can be tilted to image the prostate while minimizing attenuation (*i.e.*, above the buttocks and below the stomach, see Fig. 1b), but the gantry allows zero tilt for thin patients. A patient of average size is not fully encircled in 2D, which results in irregular and incomplete sampling due to the side gaps. Despite this incomplete sampling, we are able to reconstruct nearly artifact free images in the region of interest by using an iterative reconstruction algorithm [13].

The camera design also includes shielding [13], as shown in Fig. 1b. Inter-module septa extend 5 cm beyond the scintillator crystals to reduce background events from random coincidences and from photons that Compton scatter in the patient [14]. These septa have not yet been built, so we have operated in septa-less 3D mode for the data presented here. Lead shields are used on the ends to reduce activity from outside the field of view.

B. Electronics

Our camera uses modified commercial components in a novel geometry. We use 80 CTI ECAT HR+ block detectors that are three attenuation lengths thick for good detection efficiency with narrow detector elements (*i.e.*, 8 x 8 arrays of 4.5 x 4.5 x 30 mm^3 BGO crystals) to achieve good spatial resolution. We use modified front end, coincidence, and readout electronics developed by CTI for the HRRT brain imaging PET camera, as shown in Fig. 2. Since we are creating a non-standard camera with HR+ and HRRT components, a custom conversion board reroutes PMT signals to electronics channel inputs. Events are detected and assigned an arrival time, the crystal of interaction is identified, energy qualification is performed, and a digital word is formed using 28 CTI HRRT Analog Subsection boards. The output signals from the Analog Subsection boards are then multiplexed by six custom Detector Head Interface (DHI) boards, which are based on the CTI HRRT DHI design but each services a maximum of 15 (rather than 117) detector modules. We use six DHI boards to allow coincidences between detector modules within the same bank and plane. A CTI Coincidence Processor identifies singles events in the different DHI boards that are in coincidence, and the output is sent to a Pentium-based computer system for reconstruction and display.

C. Gantry

The PET camera is complete except for the construction of the septa. Fig. 3 shows a photograph of the camera with the lead shielding on one side removed and a single row of detector modules visible. Each detector module points toward the center of the camera, as discussed in Section IIA. The upper bank is mounted onto an aluminum back-plate whose vertical motion is controlled using a hand-crank, allowing upward movement for patient access and downward motion to maximize sensitivity. A second hand-crank is used to adjust the overall tilt of both upper and lower banks. The readout electronics are mounted on the right housing (within the Unistrut frame visible on the right in Fig. 3b). The six DHI boards are mounted horizontally to the housing that holds their corresponding Analog Subsection boards. The Coincidence Processor board is mounted onto the cabinet door for compactness. The ±5V and high voltage power supplies are mounted on the left housing.

III. Performance

A. Sensitivity and Count Rate

Coincidence event rates were measured by scanning a 1.5 mm diameter 120 μCi ^{68}Ge point source along the central axis of the patient port in 3 mm steps. A 270 keV energy threshold was used for all measurements with a 22 nsec coincidence timing window. Figure 4 shows the system sensitivity as a function of axial position. The peak absolute sensitivity is 1010 cps/μCi (2.7%) in 3D mode. This is equivalent to the peak absolute sensitivity of the EXACT HR in 3D mode and approximately 8 times higher than the

EXACT HR in 2D mode, even though our camera has one-quarter as many detectors.

The count rate as a function of activity density was measured using a 19 cm inner diameter by 19 cm long cylindrical phantom filled with ^{18}F and centered in the camera. Data were collected in 3D mode for 10 seconds every 20 minutes over a time span of 12 half-lives. Figure 5a shows the count rate as a function of activity density for total, prompt, random and true+scatter coincident events. The maximum total count rate was 1.2 Mhz at an 1.5 μCi/ml activity density. Figure 5b shows the count rate at only the lower activity density corresponding to a standard clinical range. The trues+scatter events cross the randoms at 0.23 μCi/ml.

B. Reconstruction Algorithm

We have developed a penalized maximum likelihood reconstruction algorithm for the prostate camera. The reconstruction software is designed to be very flexible in modeling arbitrary scanner geometry. Forward and back projections at each iteration are calculated using the exact position and orientation of each detector block without any rebinning. The crystal penetration effect is modeled using a geometric calculation technique similar to that presented in [15] for a positron emission mammography scanner. The attenuation correction factors are calculated based on the measured phantom geometry and a uniform attenuation coefficient of 0.095/cm. A pixel size of 2 mm is used. We estimate and subtract the random background using the standard delayed window technique. The reconstruction algorithm [13], including the normalization procedure, is not yet final so we present only preliminary results.

C. Reconstructed Images

Rectangular planar phantoms are used for normalization. Coincident data are acquired with a 27″ x 4″ x 0.375″ planar phantom centered between the detector banks (*i.e.,* placed horizontally in Fig 3b), in order to correct for coincident events that occur between detector banks. Coincident data are acquired separately with a 10.6″ x 4″ x 0.375″ planar phantom placed perpendicular to the 27″ phantom (*i.e.,* placed vertically in Fig 3b), in order to correct for coincident events that occur within the same detector bank.

Figure 6a shows a 37-point phantom. Single point sources are placed 2, 4, 6 and 8 cm from the central point. Clusters of 4 point sources are placed radially at 4 and 8 cm from the central point, and the points in each cluster are spaced 8, 6, 5 and 4 mm apart. Figure 6b shows the preliminary reconstructed image of this 37-point phantom when filled with ^{18}F at an initial activity of 0.6 mCi and imaged for two minutes. Increased blurring is seen for point sources placed further from the center. This blurring is primarily caused by missing projections, because the crystal penetration effect is modeled in the projection matrix. Minimal blurring is seen in the 10 cm diameter central region. We are able to resolve point sources that are separated by 4 mm when placed at a diameter of 8 cm and 16 cm.

Figure 7a shows a concentric-cylinder phantom with three times higher activity density in the inner cylinder than the outer cylinder. Figure 7b shows the reconstructed image of this phantom when filled with ^{18}F at an initial total activity density of 0.4 μCi/ml and imaged for four minutes. We can clearly visualize a "prostate" in a simple phantom, when the "prostate" has a three times higher activity density than the "body." Imperfect normalization factors result in some noticeable streak artifacts. We expect the results to improve once detector efficiency drifts have been minimized. Artifacts at the top and bottom of the image are due to incomplete sampling from the detector bank gaps.

IV. Discussion

PET radiopharmaceuticals have recently demonstrated promising results in the sensitive detection of prostate cancer. Initially we plan to image using [^{11}C]choline. In the future, this camera can be used to evaluate new prostate cancer radiopharmaceuticals. The high sensitivity of this new design can achieve clinical imaging wherein short duration scans are needed to avoid bladder background accumulation of tracers.

Accurate patient positioning is critical due to the limited (8 cm) axial extent of the camera. The prostate is visible in ultrasound images acquired with an external or trans-rectal transducer, and we plan to use these images to position the patient bed.

Finally, it is difficult to identify features other than the prostate and the bladder in the PET images. Local anatomic information is highly desirable to determine the location of the disease within the prostate, as well as to determine whether the disease has spread to the prostate bed. This information could be obtained with dual modality imaging. X-ray CT provides excellent images of the abdomen, but the cost is relatively high. Ultrasound imaging with a trans-rectal probe provides reasonable detail in the region of the prostate and the cost of an ultrasound unit is significantly less than that of a CT unit. We plan to explore adding co-registered ultrasound imaging capability, including the use of dual imaging for *in situ* guided biopsy.

V. Conclusion

Promising new PET tracers for prostate cancer, such as [^{11}C]choline and [^{11}C]acetate, have motivated us to build a PET camera optimized for prostate imaging. Reconstructed images of extended and point source phantoms demonstrate the feasibility of imaging prostate tumors with good spatial resolution and image contrast at low cost relative to commercial whole body PET scanners. The same sensitivity as ECAT HR in 3D mode is achieved using only one-quarter the number of detector modules and an axial length of 8 cm. Before the camera is ready for patient imaging, we still need to build the septa, automate the calibration procedure, finalize the reconstruction algorithm, and characterize the camera following NEMA performance measurements.

VI. Acknowledgment

We thank Dr. Ronald Nutt from CPS Innovations for providing detectors and electronics. This work was supported in part by the Director, Office of Science, Office of Biological and Environmental Research, Medical Science Division of the U.S. Department of Energy under Contract No. DE-AC03-76SF00098, in part by Department of Defense grant number DAMD17-02-1-0081, and in part by National Institute for Biomedical Imaging and Bioengineering grant number R01 EB 00194. Reference to a company or product name does not imply approval or recommendation by the University of California or the U.S. Department of Energy to the exclusion of others that may be suitable.

VII. References

1. J. Kurhanewicz, D. B. Vigneron, H. Hricak, et al., "Three-dimensional H-1 MR spectroscopic imaging of the in situ human prostate with high (0.24-0.7-cm3) spatial resolution," *Radiology*, vol. 198, pp. 795-805, 1996.
2. J. Kurhanewicz, D. B. Vigneron, R. G. Males, et al., "The Prostate: Magnetic Resonance Imaging and Spectroscopy: Present and Future," in *Radiologic Clinics of North America*, H. Hricak and P. R. Carroll, Eds. New York, New York: W. B. Saunders Co., 2000, pp. 115-138.
3. T. Hara, N. Kosaka, N. Shinoura, et al., "PET imaging of brain tumor with [methyl-C11]choline," *J Nucl Med*, vol. 38, pp. 842-7, 1997.
4. N. Shinoura, M. Nishijima, T. Hara, et al., "Brain tumors: detection with C-11 choline PET," *Radiology*, vol. 202, pp. 497-503, 1997.
5. T. Hara, N. Kosaka, and H. Kishi, "PET imaging of prostate cancer using carbon-11-choline," *J Nucl Med*, vol. 39, pp. 990-5, 1998.
6. T. Hara, N. Kosaka, T. Kondo, et al., "Imaging of brain tumor, lung cancer, esophagus cancer, colon cancer, prostate cancer, and bladder cancer with [C-11]choline," *J Nucl Med*, vol. 38 (suppl), pp. 250P (abstract), 1997.
7. T. Hara, K. Inagaki, N. Kosaka, et al., "Sensitive detection of mediastinal lymph node metastasis of lung cancer with 11C-choline PET," *J Nucl Med*, vol. 41, pp. 1507-13, 2000.
8. I. J. Jong, T. H. Que, J. Pruim, et al., "Imaging of bladder cancer using carbon-11 choline positron emission tomography," *J. Nucl. Med.*, vol. 41 (5 Suppl), pp. 74, 2000.
9. J. Kotzerke, J. U. Prang, B. Neumaier, et al., "Carbon-11 choline positron emission tomography (PET) of prostate cancer -- first clinical experience," *J. Nucl. Med.*, vol. 41 (5 Suppl), pp. 74, 2000.
10. J. Kotzerke, J. Prang, B. Neumaier, et al., "Experience with carbon-11 choline positron emission tomography in prostate carcinoma," *Eur J Nucl Med*, vol. 27, pp. 1415-9, 2000.
11. T. R. Degrado, R. E. Coleman, S. W. Baldwin, et al., "Fluorine-18 fluorocholine (FCH) as an oncological PET tracer: evaluation in murine prostate cancer xenograft model," *J. Nucl. Med.*, vol. 41 (5 Suppl), pp. 231, 2000.
12. T. R. Degrado, R. E. Coleman, S. Wang, et al., "Synthesis and Evaluation of F18-labeled Choline as an Oncologic Tracer for Positron Emission Tomography: Initial Findings in Prostate Cancer," *Cancer Research*, vol. 61(1), pp. 110-117, 2001.
13. J. S. Huber, S. E. Derenzo, J. Qi, et al., "Conceptual Design of a Compact Positron Tomograph for Prostate Imaging," *IEEE Trans Nucl Sci*, vol. NS-48, pp. 1506-1511, 2001.
14. J. Qi, J. S. Huber, R. H. Huesman, et al., "Septa Design for a Prostate Specific PET Camera," *IEEE Trans Nucl Sci*, vol. NS-51, pp. In Press, 2004.
15. R. H. Huesman, G. J. Klein, W. W. Moses, et al., "List mode maximum likelihood reconstruction applied to positron emission mammography with irregular sampling," *IEEE Trans Med Imag*, vol. 19, pp. 532-537, 2000.

Figures:

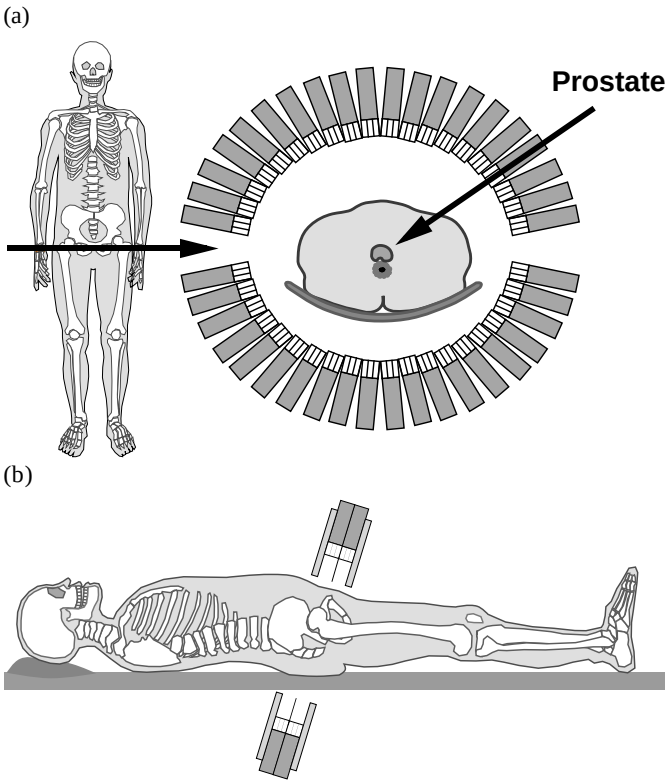

Fig. 1: Positron tomograph for prostate imaging. (a) Drawing of a transaxial view through prostate, showing the patient centered between two detector banks. The individual detector modules are angled to point towards the prostate. No shielding is shown. (b) Drawing of the sagittal view. The bottom arc is fixed below the patient bed, whereas the top arc adjusts vertically for patient access and compactness. Both detector banks are tilted and positioned as close as possible to the prostate, which improves sensitivity and minimizes attenuation. The septa and lead shielding are shown.

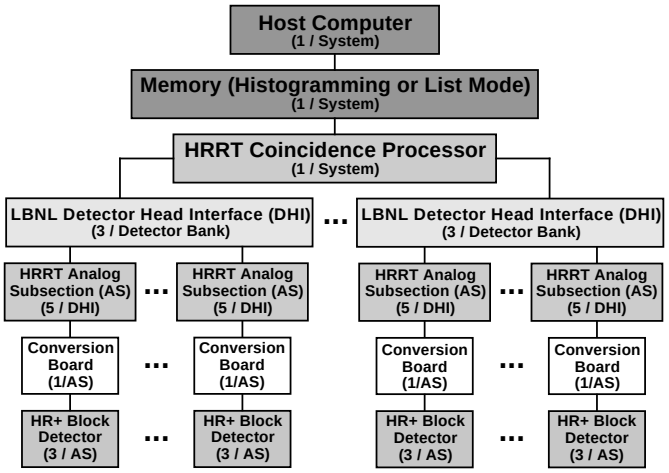

Fig. 2: Diagram of the complete data collection chain, showing the custom LBNL and CTI components and their inter-relations. The camera will use 80 CTI ECAT HR+ block detectors, 28 LBNL conversion boards, 28 CTI HRRT Analog Subsection boards, 6 LBNL custom Detector Head Interface boards, 1 CTI Coincidence Processor and a PC.

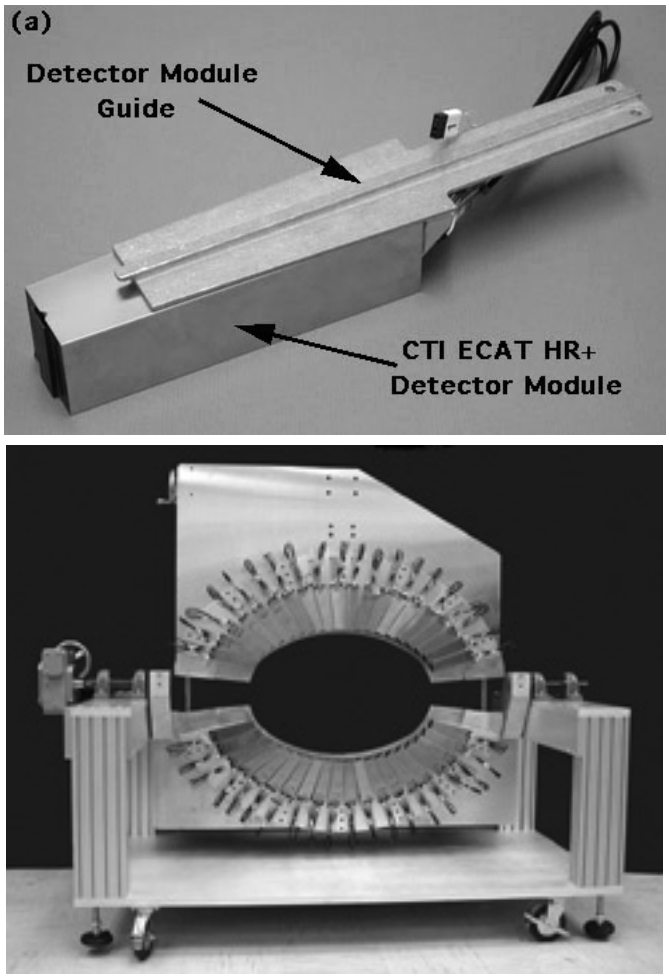

Fig. 3: (a) CTI ECAT HR+ detector module with an aluminum guide epoxied along its midline (that is used to position and secure the module). (b) Photograph of the partially-assembled camera with a single axial row of detector modules visible. The detector modules are individually angled to point towards the center of the camera. The gantry is now complete and fully loaded with electronics and shielding. The camera is complete expect for the septa.

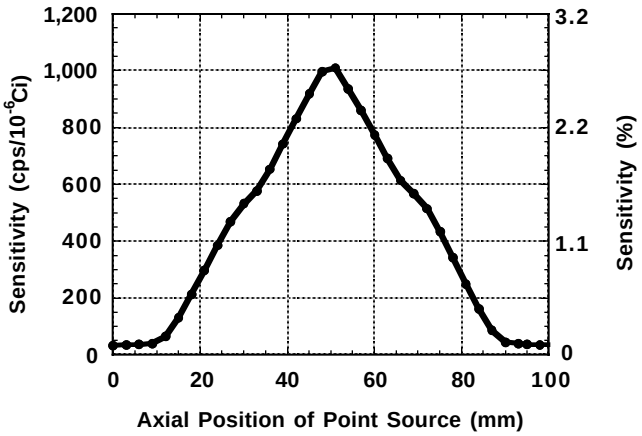

Fig. 4: System sensitivity as a function of axial position, using an 120 μCi ^{68}Ge point source. Peak absolute sensitivity in the center of the field of view is 1010 cps/μCi (2.7%) in 3D mode, which is the same as an EXACT HR in 3D mode but with one-quarter as many detector modules. Data was collected using a 270 keV energy threshold.

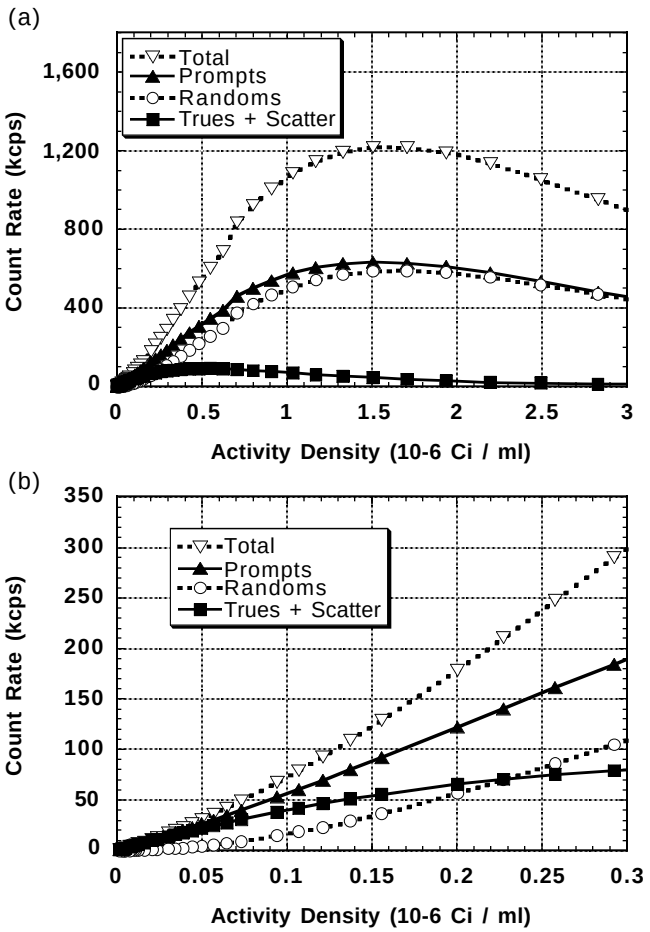

Fig. 5: Count rate as a function of activity density for total, prompt, random and true+scatter coincident events acquired with a cylindrical phantom (19 cm ID, 19 cm length) filled with ^{18}F and centered in the camera. Plots show two different ranges of activity density.

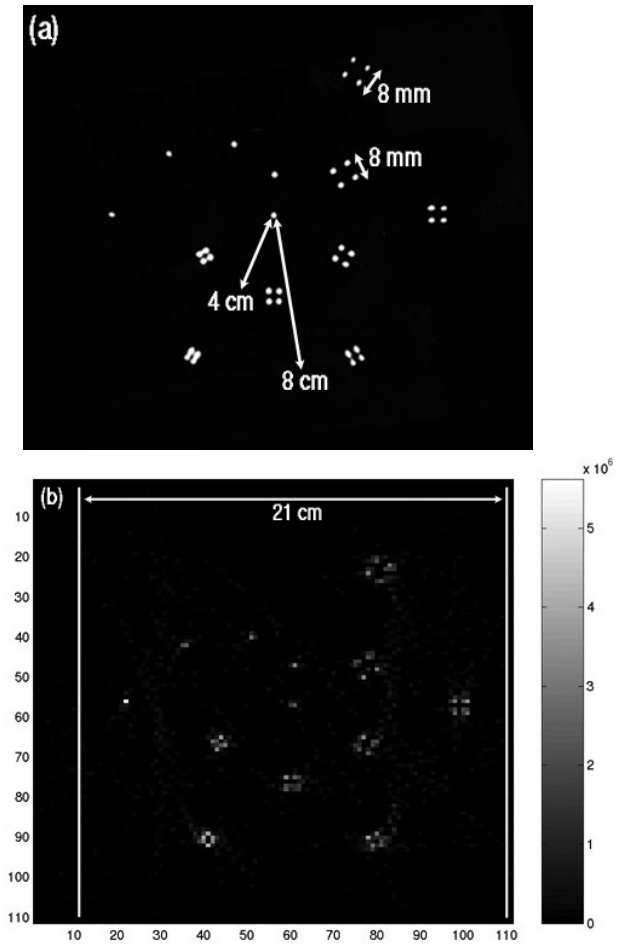

Fig. 6: (a) Drawing of a cylindrical phantom (21 cm diameter, 5 cm axial) with 37 point sources. The single point sources are 2, 4, 6, and 8 cm from the central point. Clusters of 4 point sources are placed radially at 4 and 8 cm from the central point. The 4 point sources in each cluster are spaced 8, 6, 5, and 4 mm apart (clockwise from the 8 mm labeled clusters). (b) Reconstructed image of the phantom using a preliminary iterative penalized ML algorithm. Phantom was filled with ^{18}F at an initial activity of 0.6 mCi and imaged for 2 minutes. The central point was placed in the center of the camera. Image represents 10 Mcounts. Axes are labeled in pixels (2 mm).

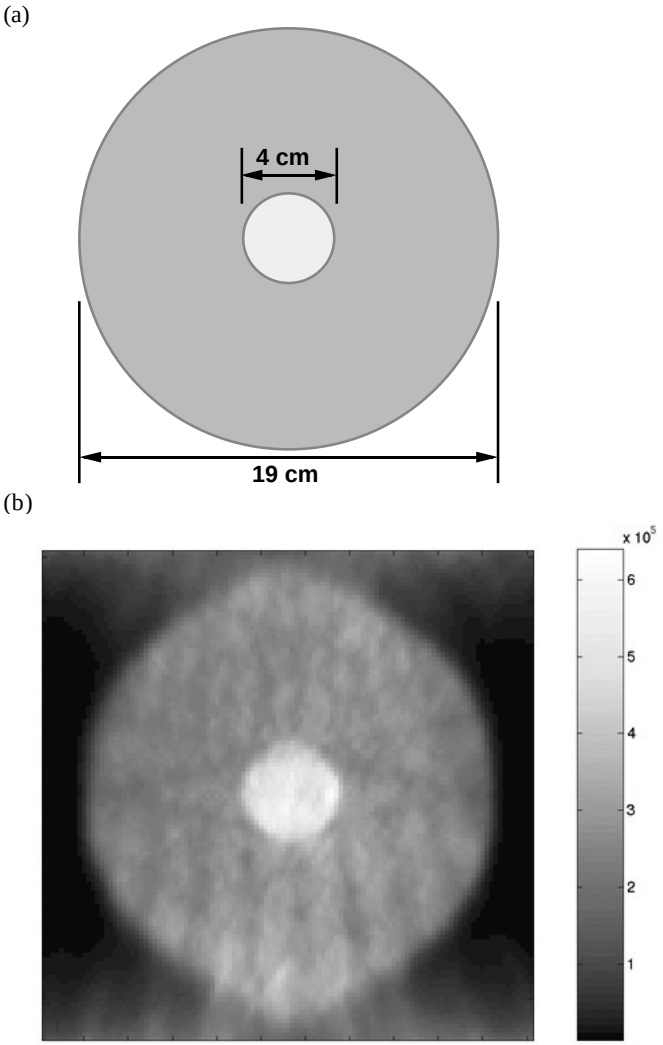

Fig. 7: (a) A concentric-cylinder phantom with three times higher activity density in the central cylinder than the outer cylinder. (b) Preliminary reconstructed image of the phantom using an iterative penalized ML algorithm. Initial total ^{18}F activity density was 0.4 μCi/ml and the imaging time was 4 minutes. Image represents 78 Mcounts.